The Astrophysical Journal, 965:142 (12pp), 2024 April 20 https://doi.org/10.3847/1538-4357/ad2fb5

Investigating Ionization in the Intergalactic Medium

Brad Koplitz, Anjali Ramesh, and Sanchayeeta Borthakur
School of Earth & Space Exploration, Arizona State University, 781 Terrace Mall, Tempe, AZ 85287, USA; brad.koplitz@asu.edu
Received 2023 October 11; revised 2024 February 20; accepted 2024 March 1; published 2024 April 16

Abstract

The intergalactic medium (IGM) contains >50% of the baryonic mass of the Universe, yet the mechanisms responsible for keeping the IGM ionized have not been fully explained. Hence, we investigate ion abundances from the largest blind QSO absorption catalog for clouds that show C IV, N V, and O VI simultaneously. The wavelength range of present UV spectrographs, however, makes it possible to probe C IV and O VI only over a small range of redshift ($z \approx 0.12$–0.15). As a result, we only have five IGM absorbing clouds, yet these provide a powerful and representative tool to probe the IGM ionization state. We found one cloud to be in collisional ionization equilibrium while three of the five showed signs of being produced by nonequilibrium processes, specifically conductive interfaces and turbulent mixing layers. None of the models we explore here were able to reproduce the ionization state of the remaining system. Energetic processes, such as galactic feedback from star formation and active galactic nucleus winds, would be excellent candidates that can cause such widespread ionization.

Unified Astronomy Thesaurus concepts: Intergalactic medium (813); Quasar absorption line spectroscopy (1317); Collisional processes (2286); Photoionization (2060)

1. Introduction

Most of the baryonic matter in the Universe is not contained in stars and galaxies, but is between galaxies in a dilute, multiphase, ionized gas called the intergalactic medium (IGM; Meiksin 2009; McQuinn 2016). This reservoir is thought to regulate the growth of galaxies by facilitating accretion (e.g., Kereš et al. 2005; Dekel & Birnboim 2006; Dekel et al. 2009; Hafen et al. 2022; Decataldo et al. 2023) and harboring a large fraction of the matter that gets ejected through outflows (e.g., Martin 1999; Martin et al. 2010; Steidel et al. 2010; Peeples et al. 2014; Oppenheimer et al. 2016). Many studies of this diffuse gas have been done at intermediate redshifts ($z \approx 2$–5) to allow for the simultaneous detection of multiple Lyman transitions of hydrogen as well as metals such as C IV or O VI (e.g., Bergeron et al. 1994; Jannuzi et al. 1998; Lopez et al. 1999; Richter et al. 2004; Simcoe et al. 2004; Adelberger et al. 2005; Chen et al. 2005; Danforth & Shull 2008; Turner et al. 2014; Morrison et al. 2021; Borthakur 2022).

Metals, in particular, are an import tracer of this diffuse gas as 70% of Lyα forest absorbers are found to have accompanying metal lines (Simcoe et al. 2004) and can be present even when the Lyman series is weak (Danforth et al. 2016). The IGM at $z \approx 2$–3 is also known to be enriched with carbon and oxygen (e.g., Davé et al. 1998; Aracil et al. 2004; Pieri et al. 2006) and is thought to have retained these and other metals to the present day (e.g., Richter et al. 2004; Aguirre et al. 2008; Danforth & Shull 2008; Tripp et al. 2008; Muzahid et al. 2012; Danforth et al. 2016). Additionally, metal absorption lines are often unsaturated, allowing for more components within a single cloud to be detected (e.g., Chen & Mulchaey 2009; Danforth et al. 2016; Pachat et al. 2017; Sankar et al. 2020; Ahoranta et al. 2021). This makes metals a key window into the ionization processes that govern the IGM.

Furthermore, analyzing metals has revealed the multiphase nature of the IGM (e.g., Heckman et al. 2002; Savage et al. 2005; Narayanan et al. 2009; Shull et al. 2012; Ahoranta et al. 2021; Haislmaier et al. 2021), with a cool $T \approx 10^{4.5}$ K phase and a warm-hot phase, known as the warm ionized IGM or WHIM, at $T \approx 10^5$–10^6 K. The presence of the WHIM could indicate that collisions are likely a dominate ionization process in the IGM since many of these processes produces radiatively cooling gas at the intermediate temperatures O VI is found at (e.g., Begelman & Fabian 1990; Heckman et al. 2002; Gnat et al. 2010; Kwak et al. 2015; Ji et al. 2019), although multiple studies have assumed photoionization equilibrium (PIE) or collisional ionization equilibrium (CIE) to estimate IGM masses and densities (e.g., Lehner et al. 2007; Sobacchi & Mesinger 2013).

In the largest, most complete IGM survey to date, Danforth et al. (2016) identified 5138 extragalactic absorption features along 82 QSO sight lines taken with the Cosmic Origins Spectrograph (COS) onboard the Hubble Space Telescope (HST; Osterman et al. 2011; Green et al. 2012) with signal-to-noise ratios (S/Ns) above 15. They grouped features found at similar redshifts into 2611 absorbing systems. 16% of these had at least one metal line, with O VI being most frequently detected, similar to what other studies have found in the local Universe (e.g., Danforth & Shull 2008; Tilton et al. 2012). The number of absorbers per unit z ($\frac{d\mathcal{N}}{dz}$) of O VI and H I were found to increase with z; however, this was not seen for N V, C III, or Si III, which do not seem to evolve (Danforth et al. 2016).

Despite the progress that has been made, it is still unclear whether this diffuse gas is in ionization equilibrium—photoionization or collisional ionization—or if nonequilibrium processes are needed to explain observations. To that end, we have analyzed the absorption features from Danforth et al. (2016), which allow us to constrain the physical processes driving ionization in the IGM in the context of equilibrium and nonequilibrium interactions. The rest of this paper is outlined as follows: Section 2 details how our sample was selected as well as the measurements used in our analysis. Section 3 presents the analysis and the results from it. Finally, we summarize in Section 4 and discuss future directions.

2. Sample and Measurements

2.1. Sample Selection

The presence of high-ionization transitions can be used to constrain the physical nature of the IGM. In particular, warm-hot metals such as C IV ($\lambda\lambda$1548, 1550; 64.5 eV), N V ($\lambda\lambda$1238, 1242; 97.9 eV), and O VI ($\lambda\lambda$1032, 1038; 138.1 eV), trace the energies required to ionize the IGM and provide a unique window into some of the commonly observed nonequilibrium processes that are most likely responsible for the ionization state of the IGM. To that end, we consider all absorbing clouds (i.e., sets of absorption features which are aligned in velocity space) from Danforth et al. (2016)'s Mikulski Archive for Space Telescopes (MAST) catalog[1] and examine those with 3σ detections of these three ions. While it is possible that absorption features are kinematically aligned by chance and not actually associated with one another, the likelihood is very small when multiple ions are found at similar velocities. As a result, we assume all kinematically aligned ions originate from a single absorbing cloud.

The selection criteria yield five clouds along four sight lines that showed absorption in all three transitions. Each of these clouds were best fit by a single Voigt profile or component. The sight line of PG 1216+069 contained two clouds with a velocity separation ~ 75 km s^{-1}. Although Danforth et al. (2016) identified them as independent, these could be associated with a larger structure.

Even though only five absorbing clouds from the Danforth et al. (2016) catalog are included in our complete sample, these are representative of the IGM. The small number can be attributed to the narrow z-range within which C IV and O VI can be simultaneously observed using COS. At minimum, z needs to be $\gtrsim$0.094 to have at least one O VI feature within the G130M grating, and $z \gtrsim 0.100$ to observe the stronger 1032 Å line. Meanwhile, any cloud with $z \gtrsim 0.153$ will have both C IV features shifted out of the G160M grating. Only 341 clouds were within the allowable range, limiting the number that could have been included. Most of these only contained Lyα with no associated metal features (246 of 341). O VI, the most frequently detected metal, appeared in 44 individual clouds ($\mathcal{N}$), implying $\frac{d\mathcal{N}}{dz}$(O VI) ≈ 9, which is comparable to what Danforth & Shull (2008) found for O VI (15^{+3}_{-2}). The fact that the 82 QSOs from Danforth et al. (2016) are randomly distributed across the sky indicates that these absorbers are likely more prevalent than the small sample size would imply.

2.2. Voigt Profile Measurements

We fit Voigt profiles to the absorption features to determine the column density (N), Doppler width (b), and relative velocity or velocity centroid ($v_{\rm obs}$) of the absorbing gas and check for consistency with the analysis of Danforth et al. (2016). In addition, Danforth et al. (2016) fit each absorption profile individually whereas we fit doublets, such as C IV and O VI, simultaneously. Before fitting, we normalized the continuum within $\pm$600 km s^{-1} of the cloud's z, which we refer to as $z_{\rm sys}$, and center the features such that $v_{\rm obs}$ is always near 0 km s^{-1}. The absorption features were fit using a reduced χ^2 algorithm (Sembach & Savage 1992). Once complete, these Voigt profile parameters can be used to constrain the ionization processes happening in the IGM. We show the spectrum and associated fits of this analysis for the four sight lines in the Appendix.

We present the absorber properties used in our analysis in Table 1. The $v_{\rm obs}$ returned by our fits are not reported since each was centered on $z_{\rm sys}$ before fitting. If the best-fit Doppler width (b) of an absorber is narrower than 5 km s^{-1}, we fix b to 5 km s^{-1} and report the resulting column density (N). This is motivated by the COS line-spread function since it is unable to

[1] https://archive.stsci.edu/prepds/igm/

Table 1
Summary of Measurements

QSO (1)	$z_{\rm sys}$ (2)	Ion (3)	log (N/cm^{-2}) (4)	b(km s^{-1}) (5)
(1) PG 1116+215	0.13853	H I	15.30 ± 0.03	28.9 ± 1.0
		Si II	12.93 ± 0.04	⩽5[a]
		Si III	13.73 ± 1.31	5.8 ± 1.9
		C II	13.98 ± 0.13	8.6 ± 1.3
		Si IV	12.83 ± 0.20	5.9 ± 4.2
		C IV	13.40 ± 0.09	⩽5[a]
		N V	12.78 ± 0.06	15.0 ± 1.2
		O VI	13.82 ± 0.02	30.8 ± 1.1
(2) PG 1216+069	0.12360	H I	14.63 ± 0.05	22.8 ± 1.1
		Si II	<11.88	…
		Si III	12.53 ± 0.21	7.3 ± 2.9
		C II	<12.93	…
		Si IV	12.71 ± 0.11	19.5 ± 2.6
		C IV	14.24 ± 0.24	10.4 ± 1.3
		N V	13.42 ± 0.09	⩽5[a]
		O VI	14.19 ± 0.05	20.2 ± 1.4
(3) PG 1216+069	0.12389	H I	14.86 ± 0.06	24.96 ± 1.1
		Si II	<11.88	…
		Si III	12.51 ± 0.10	⩽5[a]
		C II	<12.93	…
		Si IV	12.84 ± 0.12	⩽5[a]
		C IV	13.99 ± 0.15	11.0 ± 1.3
		N V	13.04 ± 0.12	10.4 ± 13.6
		O VI	14.19 ± 0.06	32.0 ± 1.4
(4) PG 1424+240	0.14713	H I	15.56 ± 0.12	27.5 ± 1.1
		Si II	<11.78	…
		Si III	14.31 ± 1.21	5.4 ± 1.7
		C II	<12.82	…
		Si IV	12.99 ± 0.16	7.8 ± 2.7
		C IV	14.24 ± 0.16	14.4 ± 1.3
		N V	13.16 ± 0.16	33.6 ± 1.9
		O VI	14.07 ± 0.43	⩽5[a]
(5) PKS 0637–752	0.12288	H I	15.36 ± 0.40	30.5 ± 1.2
		Si II	<11.74	…
		Si III	14.05 ± 1.18	8.2 ± 1.7
		C II	<12.86	…
		Si IV[b]	…	…
		C IV	13.65 ± 0.04	38.8 ± 1.2
		N V	14.05 ± 0.04	71.9 ± 1.1
		O VI	14.08 ± 0.03	44.0 ± 1.1

Notes. Column (1) shows the quasar toward the system. Column (2) is the redshift of the system. Column (3) indicates the ion being fit. Columns (4) and (5) are the column density and Doppler width of the ion in units of cm^{-2} and km s^{-1}, respectively.

[a] Doppler width was fixed at 5 km s^{-1} due to the absorption line being narrow. See Section 2.2 for details. It is worth noting that these features are consistent with extremely narrow ($b \ll 5$ km s^{-1}) features, implying large column densities. Measurements that are consistent with CIE models (Gnat & Sternberg 2007) are highlighted with a bracket.

[b] Both transitions fell within a gap in the data, so a fit could not be completed.

discern between b-values $\leqslant 5$ km s^{-1} at a S/N between 10 and 20. This is a limitation of the data. It is possible for these clouds to be associated with an extremely low Doppler width and a much higher column density. Most of our measurements were consistent with those from Danforth et al. (2016) and so we adopt our values. We also fit the Si IV ($\lambda\lambda$1393, 1402; 45.1 eV) features of our clouds as they provide an additional probe of the ionization mechanisms; however, we do not include the ion in our selection criteria as it may not completely trace the WHIM as indicated by its low ionization potential (Cen & Ostriker 1999; Davé et al. 2001; Cen & Ostriker 2006; McQuinn 2016). The lower ions Si II ($\lambda\lambda\lambda$1260, 1193, 1190; 16.4 eV), C II (λ1334; 24.4 eV), and Si III (λ1260; 33.5 eV) were also fit when detected. If no absorption is present, we measure twice the error of the rest-frame equivalent width within a 100 km s^{-1} window that does not contain intervening absorption. This is then converted to an upper limit on N, assuming we are in the linear portion of the curve of growth. Neither absorbing cloud along the sight line to PG 1216+069 contained Si II or C II, so we report the same upper limits for both clouds.

Any Voigt profile analysis is limited by the resolution of the spectrograph used. The COS instrument currently has the highest spectral resolution at rest-frame far-ultraviolet wavelengths that could observe the QSOs in the Danforth et al. (2016) sample. However, it is important to note that it is a medium resolution instrument ($R \approx 20{,}000$; FWHM $\approx$15 km s^{-1}). Thus, it is possible that multiple narrow clouds at similar velocities could appear as a single, wider component. We assume that the measurements presented here are dominated by the largest absorbing cloud with the understanding that higher-resolution observations may reveal a more complicated picture.

2.3. Comparison to Literature Measurements

Many of the clouds we analyze here have been identified by other studies and fit many of the same transitions as us. We compare our measurements to those in the literature below.

In the system along the sight line to PG 1116+215, Sembach et al. (2004), Tripp et al. (2008), Tilton et al. (2012), and Muzahid et al. (2018) found similar values of log$N$ and b to what we measure for most metals. However, Tilton et al. (2012) found larger log$N$ values for H I and N V than our fits ($\sim$0.4 and $\sim$1 dex more, respectively). Muzahid et al. (2018) found the log$N$ of H I to be larger than we report while finding less C IV. The fit from Sembach et al. (2004) gave a larger log$N$ and smaller b than us. Meanwhile, Tripp et al. (2008) fit the H I absorption as two components, both of which have narrower b and larger log$N$ values than we find.

As discussed in Section 2, the small velocity separation of the two absorbing clouds toward PG 1216+069 could cause them to be treated as one system, which is what Tripp et al. (2008), Chen & Mulchaey (2009), and Tilton et al. (2012) have done. Tripp et al. (2008) found values for O VI which are consistent with what we measure. Their H I measurements for the system at $z = 0.12360$ are consistent with what we find, though they find a larger log$N$ and smaller b than we do for system 3 at $z = 0.12389$. The O VI features measured by Chen & Mulchaey (2009) have similar, but inconsistent, log$N$ as we find while their b-value of the system at $z = 0.12360$ is narrower. For Si III, Chen & Mulchaey (2009) set $b = 2.4$ km s^{-1} and found the corresponding best-fit log$N$, which is consistent with what we find. The H I features of both clouds were reported as lower limits, which are consistent with the system at $z = 0.12360$ but not the system at $z = 0.12389$; however, Lyβ was not included in their fits, which may have impacted this. Tilton et al. (2012) measured similar log$N$ and b-values for O VI in both systems.

For the PG 1424+240 system, Muzahid et al. (2018) measured log$N$ values for C IV and O VI that are consistent with what we find. However, they measured larger values of log$N$ for H I, C II, and Si II than we do. Part of the difference in H I can likely be attributed to how the values are reported. They report a total log$N$ of H I from a fit with four components while we fit the feature with two components and only report the value of the single cloud which is kinematically aligned with the associated metal lines. The discrepancy for the C II and Si II features can be attributed to how the lines were identified. Danforth et al. (2016) labeled these as weak H I absorbing clouds, and so we report an upper limit for these metals where Muzahid et al. (2018) fit Voigt profiles.

In the PKS 0637−752 system, Johnson et al. (2017) fit two components to the H I, C IV, and O VI features and one component to Si III whereas we fit a single component to all of the metals features and two components for H I. This difference caused our b-values of C IV and O VI to be larger than what they find, though we measured similar total log$N$ values for all metals. Our log$N$ value for H I is consistent with what they find, though we find a larger b-value.

3. Results and Discussion

3.1. Collisional Ionization Equilibrium Models

To determine whether the absorbing clouds we have identified are in CIE, we compare the measurements to the solar metallicity (Asplund et al. 2009) models from Gnat & Sternberg (2007). PKS 0637−752 is the only sight line that is consistent with CIE at a temperature near $10^{5.3}$ K, which we show in Figure 1. The remaining four clouds had less N V than predicted. Gatuzz et al. (2023) looked at the cloud along the PG 1116+215 sight line and concluded that it was not in CIE, consistent with what we find here.

3.2. Photoionization Equilibrium Models

The PIE code CLOUDY (v.17; Ferland et al. 2017) allows us to explore whether our measurements can be explained by an incident radiation field alone. Each model was exposed to a Haardt & Madau (2012) extragalactic UV background and was iterated until the Lyα column density was reached. The metallicities of the features in our sample are assumed to be solar (Asplund et al. 2009). To determine the total H density (log$n_{\rm H}$) of the clouds, we varied log($n_{\rm H}$/cm^{-3}) in steps of 0.1 dex from −7 to −2.

No absorbing cloud was found to be consistent with PIE models, regardless of the log$n_{\rm H}$ used. We show the measurements of the absorbing cloud toward PG 1216+069 at $z = 0.12360$ in Figure 2 as an example. This shows that there is no density consistent with the measured values for all four ions from these models (log($n_{\rm H}$/cm^{-3}) $\approx$ −4.1, −4.8, −4.9, and −5.1 for Si IV, C IV, N V, and O VI, respectively). So the absorbing cloud is not consistent with being in PIE. Changing the metallicity of the models would not impact this conclusion as this would move all of the models up or down together concurrently and would not impact their ratios. In four of the five absorbing clouds, C IV and O VI were found in similar

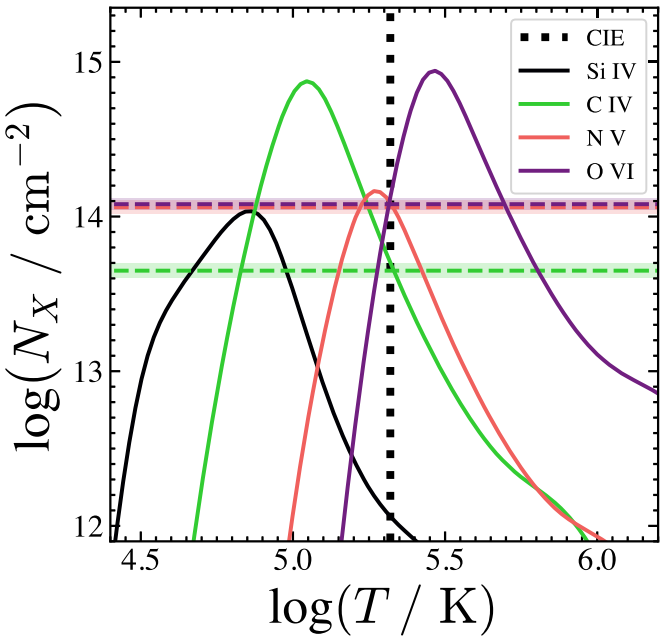

Figure 1. Comparing our measurements of the PKS 0637–752 cloud to CIE models (Gnat & Sternberg 2007). Measurements are shown as dashed lines with uncertainties as shaded regions while CIE models are shown as solid lines. The color indicates the ion being plotted, with black for Si IV, green for C IV, red-orange for N V, and purple for O VI. Both Si IV lines fell within a gap in the data and so a measurement could not be made. The black dotted line shows where the cloud is in CIE at $T \approx 10^{5.3}$ K.

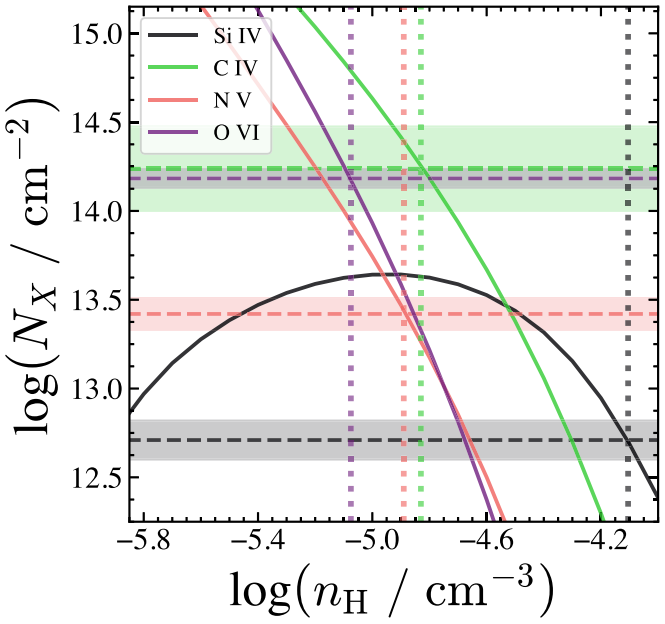

Figure 2. Comparing our measurements of the PG 1216+069 absorbing cloud at $z = 0.12360$ (system 2) to PIE models (Ferland et al. 2017). Measurements are shown as horizontal dashed lines with uncertainties as shaded regions while PIE models are shown as solid lines. The $\log n_{\rm H}$ values which best match our measurements are highlighted with vertical dotted lines. The color indicates the ion being plotted, with black for Si IV, green for C IV, red-orange for N V, and purple for O VI.

amounts, which CLOUDY was not able to match without needing significantly more N V than we measured. These show that photoionization is not the dominant ionization process for most high ions, unlike previously believed (e.g., Narayanan et al. 2009; Muzahid et al. 2011).

3.3. Nonequilibrium Models

Since only one cloud is consistent with an equilibrium model, we investigate our measurements for consistency with nonequilibrium models. Figure 3 shows the nonequilibrium models as well as the CIE and PIE models previously discussed. Below, we detail each model while comparing the expected column density ratios for solar metallicity and relative abundances to our results.

Shock ionization (SI) can occur when gas clouds move through an ambient medium at velocities above the local sound speed. In the IGM, this can be the result of galactic outflows giving clouds enough energy to escape the galaxy's dark matter gravitational potential. When this happens, the temperature gets raised behind the cloud, causing higher ionization states to be populated, which Dopita & Sutherland (1996) have modeled using clouds with varying shock velocities (150 and 500 km s^{-1}) and magnetic parameters ($0\ \mu$G cm$^{-3/2} \leqslant B_0\, n_0^{-3/2} \leqslant 4\ \mu$G cm$^{-3/2}$). These models are shown in Figure 3 in black. Most of our systems (four of the five) have C IV:O VI ratios consistent with the predicted values. However, in each case we see significantly more N V than what is expected based on the models.

RC via recombination can produce warm-hot ions as the gas temperature decreases from $>10^6$ K. By cooling gas under a variety of conditions, Edgar & Chevalier (1986) were able to predict the column density ratios one would see if RC is the dominate ionization method. The RC models for flow velocities of 100 km s^{-1} are shown in green in Figure 3. These ratios overpredict the amount of O VI we see in all of the clouds. In two clouds, we find nearly an order of magnitude more C IV than expected from the models. As a result, we conclude that RC is not a prominent ionization mechanism in these absorbing clouds.

CIs occur when media at different temperatures come into contact with each other; for example, when a cool cloud from a galaxy's interstellar medium gets ejected into the warm-hot IGM. Collisions at the contact surface will transfer energy (and temperature) to the colder gas, producing the warm-hot metals in which we are interested. Borkowski et al. (1990) modeled the contact surface between hot 10^6 K gas and cooler interstellar clouds, with the results being shown in Figure 3 in red-orange. These models vary the angle of the magnetic field orientation between 0° and 85° as well as interface ages between 10^5 and 10^7 yr. This age range suggests that these interfaces die out rather rapidly. Star-formation-driven galactic winds in starburst galaxies are known to produce high-ionization transitions such as C IV and O VI in the outer circumgalactic medium (CGM) and IGM (Adelberger et al. 2005; Borthakur et al. 2013; Heckman et al. 2017; Méndez-Hernández et al. 2022; Banerjee et al. 2023), although the nonequilibrium nature of those systems are not fully explored. Only system 3 (the cloud at $z = 0.12389$ toward PG 1216+069) is consistent with the predicted ratios in both panels of Figure 3. Meanwhile, system 1 (the cloud toward PG 1116+215) and system 2 (the cloud at $z = 0.12360$ toward PG 1216+069) are only consistent with the left and right panels, respectively, though system 2 is near the boarder in the left panel. The PKS 0637−752 cloud is in CIE and has more N V than the models predict, suggesting it may have once had a CI that has since dissipated as the cloud reached CIE. Given that the ionization potential of Si IV allows it to be produced by colder IGM gas phases than C IV or the hotter ions, we believe that the C IV measurements are a more robust tracer of the WHIM phase in the IGM. As a result, we conclude that the ionization of

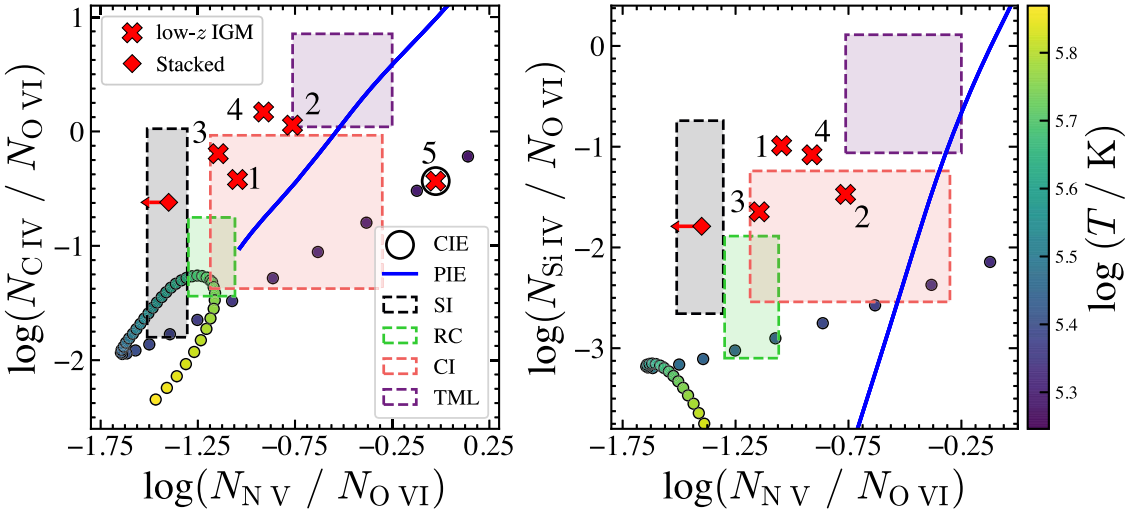

Figure 3. Comparing our measurements to various ionization models. We show our measurements for the five clouds as red stars while the final stacked spectrum is shown as a red diamond, which we discuss in Section 3.5. The measurement uncertainties were always smaller than the size of the points and so are not shown. Each cloud is label with their corresponding number from Table 1. CIE models are shown as circles with the color corresponding to the model's temperature as shown in the color bar. The black solid ring highlights the cloud toward PKS 0637–720, which is consistent with being in CIE. PIE models are shown as a solid blue line. The dashed lines indices where the different nonequilibrium ionization models are expected to reside with the coloring indicating the model, with black for shock ionization (SI), green for radiative cooling (RC), red-orange for conductive interfaces (CIs), and purple for turbulent mixing layers (TMLs). These models are discussed in Section 3.3.

systems 1, 2, and 3 can largely be explained by CIs resulting from energetic processes impacting the IGM.

When a turbulent hot gas comes into contact with a colder medium, Kelvin–Helmholtz instabilities can form, causing a mixing of different gases, which are referred to as TMLs. These layers are at high enough temperatures to produce the highly ionized species we analyze here. Slavin et al. (1993) expanded upon Begelman & Fabian (1990) to produce a model of TMLs over a range of temperatures and gas velocities. These models, which we show in purple in Figure 3, correspond to entrainment velocities between 25 and 100 km s^{-1} as well as temperatures between $10^{5.0}$ and $10^{5.5}$ K. These models stand out among those we analyze because of the large C IV:O VI and Si IV:O VI ratios predicted. The cloud along the sight line to PG 1216+069 at $z = 0.12360$ (system 2) is near the boundary of TMLs in the left panel, suggesting this is a major contributor to its ionization state in addition to CIs.

The cloud toward PG 1424+240 (system 4) does not match the predicted values for any of the models we explore here, though it is near the boarder of CIs and TMLs in both panels of Figure 3. This could indicate that these mechanisms are playing some role in the observed ionization state; however, there could other processes impacting these ion ratios. The uncertainty of the O VI log$N$ may also play a part in its positional inaccuracy in Figure 3 as discussed in Section 2.2.

To summarize these results, most of the clouds we analyze are consistent with CIs when comparing C IV measurements. Of which, one also match the predicted ratios for TMLs. This is similar to what was found for Milky Way high-velocity clouds (Fox et al. 2005). The models we investigate here are not able to reproduce the observed ratios of one system. These results indicate that the IGM may be predominantly ionized through nonequilibrium processes. More work is needed with a larger sample, however, to be able to draw more definitive conclusions.

These results could change if the relative abundances are largely different from solar values. Though this is unlikely to be the case in the absorbing clouds we investigate here given the low redshifts they reside at and no study has found strong evidence for nonsolar relative abundances in the IGM or outer CGM. Additionally, Si IV can be produced by multiple gas phases, not just the warm-hot phase. This means the placement in the right panel of Figure 3 can be thought of as an upper limit on the y-axis. The multiphase nature of Si IV does not impact the conclusions drawn here, given that the vast majority of the ion abundances would need to be produced by cooler gas phases to change our interpretations.

Table 2
Summary of Possible Ionization Sources

Sight Line (1)	z_{abs} (2)	z_{gal} (3)	R_{vir} (4)	ρ (5)	Process(es) (6)
PG 1116+215	0.13853	0.138	172	140	CI
PG 1216+069	0.12360, 0.12389	0.124	125	94	CI, TML
PG 1424+240	0.14713	0.15	81	132	⋯
PKS 0637−752	0.12288	0.1229	70	16	CIE

Note. Column (1) indicates the sight line. Columns (2) and (3) are the redshift of the absorbing cloud and the galaxy, respectively. Column (4) is the virial radius of the foreground galaxy in units of kpc. Column (5) is the projected distance between the QSO and galaxy in units of kpc. Column (6) shows the ionization processes consistent with the log$N$ ratios in Table 1.

3.4. Possible Sources of Ionization

With it being apparent from the above results that nonequilibrium processes are the dominate way to determine the ionization state of the IGM, it is important to look for the sources driving the nonequilibrium processes. Galaxies with large outflows are capable of driving clouds out of the galaxy into the CGM and IGM (Oppenheimer et al. 2012; Somerville & Davé 2015). This is why using a galaxy's virial radius as a boundary between the CGM and IGM is often insufficient or misleading, given that processes which occur at or near this border are likely to persist to further radii with little changing (e.g., Nelson et al. 2019). To determine whether or not there are galaxies near the sight lines that could be responsible for the ionization processes we infer in Section 3.1, we have performed a literature review of the absorbing clouds in our sample with the results summarized below and in Table 2. The Sloan Digital Sky

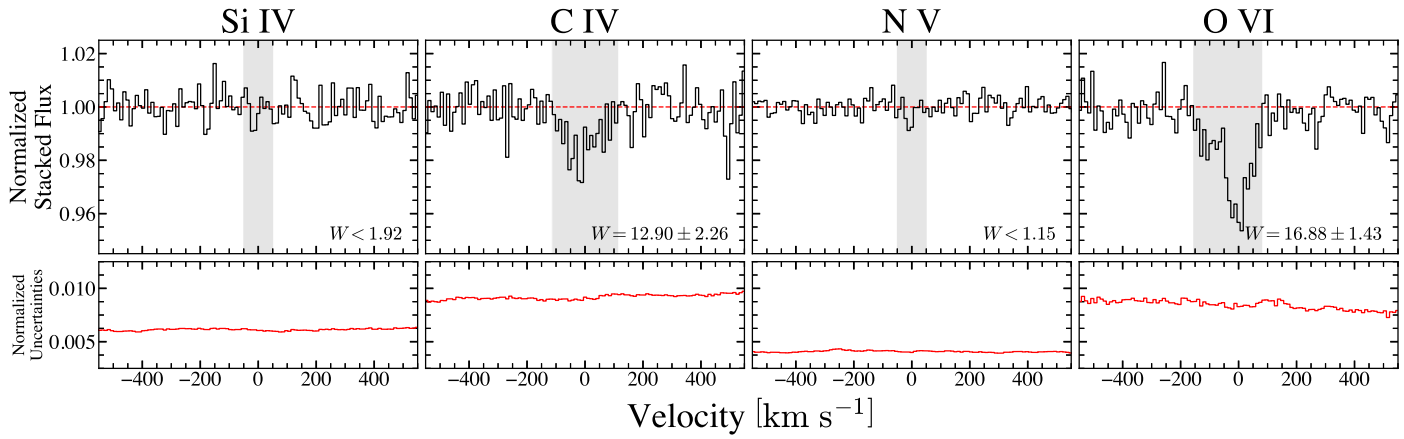

Figure 4. Stacked spectra for the expected location of Si IV (left), C IV (center left), N V (center right), and O VI (right) transitions for all IGM clouds in Danforth et al. (2016). The upper panels show the stacked flux while the bottom panels show the corresponding stacked error. The gray region indicates the range used to calculate the equivalent width, which we show in the bottom right of the upper panels in units of mÅ.

Survey and other large spectroscopic surveys are shallow at these redshifts. Thus, deeper individual surveys are needed to identify nearby galaxies.

The sight lines to PG 1116+215, PG 1216+069, and PG 1424+240 were found to pass within 140 kpc (Tripp et al. 2008; Muzahid et al. 2018; Scott et al. 2021), 94 kpc (Chen & Mulchaey 2009; Scott et al. 2021), and 132 kpc (Scott et al. 2021), respectively, of galaxies at similar redshifts as these clouds. The virial radii of these galaxies, as shown in Table 2, suggest that the sight lines to PG 1116+215 and PG 1216+06 probe the boundary between the outer CGM and IGM. Given that CIs are short-lived processes, these galaxies are likely responsible for sourcing the observed ionization in these clouds. The sight line to PG 1424+240 is the only cloud located outside the nearby galaxy's virial radius. This suggests that the absorbing cloud escaped the gravitational potential of the galaxy and interacted with the ambient IGM to produce the observed ionization.

The PKS 0637−752 sight line stands out as it is only ∼16 kpc from a galaxy at the same redshift as the cloud in our sample, putting it into the inner CGM of this star-forming dwarf galaxy ($M_\star \approx 10^{7.9}$ $M_\odot$; Johnson et al. 2017). It is especially note worthy that this is the only cloud found to be in CIE at a temperature $\sim 10^{5.3}$ K. This temperature is close to the virial temperature of this galaxy ($T \approx 10^{5.1}$ K), assuming the stellar mass to halo mass conversion of Kravtsov (2013) and a virial temperature estimation as described in Wang & Abel (2008). In this case, we are most likely observing the virialized halo of this galaxy, although heated gas from feedback processes cannot be ruled out.

3.5. Stacked Spectra

While analyzing individual absorbing clouds can tell us about the processes taking place within these few examples, stacking the spectra of many IGM clouds allows us to quantify better the average strength of the lines. We mean stacked the 341 IGM clouds, both detections and nondetections, in Danforth et al. (2016) with a redshift that allows C IV and O VI to be observed, with the results being shown in Figure 4. The spectra were centered on the z of the Lyα before stacking. After stacking all IGM clouds, we normalized the continuum using polynomials of second or third order. The errors from the individual spectra were added in quadrature to obtain the stacked spectrum errors, which we show in the bottom panel of Figure 4.

Table 3
Summary of the Stacked Spectrum

Ion (1)	W (mÅ) (2)	log (N/cm^{-2}) (3)	$v_{\rm obs}$ (km s^{-1}) (4)	$V_{1\sigma}$ (km s^{-1}) (5)
Si IV	<1.92	<11.34	...	...
C IV	13.01 ± 2.47	12.51 ± 0.05	−0.8 ± 30.58	43.0 ± 21.5
N V	<1.15	<11.73	...	...
O VI	16.88 ± 1.43	13.13 ± 0.04	−18.5 ± 12.91	85.9 ± 21.5

Note. Column (1) shows the ion being stacked. Column (2) is the equivalent width of the stacked spectrum. Columns (3) and (4) are the column density and velocity centroid of the stacked spectrum measured through the AOD method in units of cm^{-2} and km s^{-1}, respectively. Column (5) indicates the 1σ width of the stacked spectrum in units of km s^{-1}.

The log$N$ and $v_{\rm obs}$ of the stacked spectrum were constrained using the adaptive optical depth (AOD) method (Savage & Sembach 1991; Lehner et al. 2020), which we were able to use since the features included in the stacks were in the linear region of the curve of growth. The IGM line lists published by Danforth et al. (2016) contain a flag indicating whether or not the line is saturated, which we use to confirm that the clouds included in the stacks are in the linear region of the curve of growth. The AOD method uses the normalized flux in velocity space to estimate the apparent optical depth in each pixel such that $\tau_a(v) = \ln[F_{\rm cont}(v)/F_{\rm obs}(v)]$. Since we are in the linear region of the curve of growth, the apparent column density in each pixel can be found by assuming the absorber is unsaturated such that $N_a(v) = 3.768 \times 10^{14}\, \tau_a(v)/(f\lambda[\text{Å}])$ [cm^{-2} (km s^{-1})$^{-1}$]. This gives N by integrating over the velocity range of the absorber. We define the width of the stacks as half the velocity width where the normalized flux is 1σ below the continuum ($V_{1\sigma}$) after binning the spectra by 4 pixels. These results are presented in Table 3.

Weak absorption was detected in the C IV and O VI spectra at >5.5σ. No features were measured in Si IV or N V, even with the higher S/Ns. As a result, we report the upper limits for these ions as twice their associated uncertainties within ±50 km s^{-1}. While it appears by eye that narrow features are present in Si IV and N V, they were not detected at 2σ. It may not be surprising that we do not detect Si IV or N V in the stack

given that the strength of an absorption line is dictated by the product of the elemental abundance, the fraction of the element in the ionization state, and oscillator strength of the line. For the strongest transitions of C IV and O VI, the products of their abundances and oscillator strengths are similar while the products for Si IV and N V are an order of magnitude smaller (see Table 4 in Morton et al. 1988). Thus, Si IV/Si and N V/N would need to be $\gtrsim$10 times C IV/C and O VI/O for each ion to produce profiles of similar strengths.

The AOD method reveals that, on average, C IV and O VI are kinematically aligned with their associated Lyα absorbers, with $|v_{\rm obs}| < 20$ km s^{-1} in both stacks. From the individual absorbing clouds we have analyzed, we believe this trend would continue in Si IV and N V if the absorption was stronger.

We constrain the distribution of $v_{\rm obs}$ of the clouds that went into the stacks by measuring $V_{1\sigma}$ for the combined features. The widths of C IV and O VI suggest hotter ions are more likely to differ kinematically from their Lyα absorbers. We hypothesize that these are caused by gas kinematics responsible for nonequilibrium processes producing the coronal transitions.

As seen in Figure 3, the column density ratios of the stacked spectrum are consistent with only SI models. In addition, these ratios are inconsistent with PIE and CIE models, suggesting that the ionization of the IGM is frequently driven by nonequilibrium processes. This shows that while SIs do not play a major role in the individually absorbing clouds we have analyzed, they may play a part in the overall ionization of the IGM. However, it is worth noting that the stacked spectrum is not suitable for ratio studies and these results may suffer from issues with averaging multiple populations as one.

4. Summary

In this work, we explore the ionization processes responsible for the ionization of the WHIM phase of the IGM in the local Universe by analyzing absorbing clouds with C IV, N V, and O VI detected at $\geqslant 3\sigma$ from Danforth et al. (2016). Our results are summarized as follows.

1. Only one cloud was found to be in equilibrium (system 5), specifically CIE with a temperature near $10^{5.3}$ K. This sight line is also only ~16 kpc from a star-forming dwarf galaxy, hinting that the higher densities found closer to galaxies allow the diffuse halo gas to cool faster than it does further away, where the densities are lower.
2. None of the clouds were found to be consistent with PIE models, even though the IGM is frequently assumed to be in PIE. Each absorbing cloud required multiple densities to reproduce the observed abundances. In particular, these models were not able to reproduce the amount of C IV and O VI we see without needing significantly more N V than was found.
3. We compare our observations to four nonequilibrium models: SI, RC, CI, and TML. No system was found to be consistent with the expected ratios from the SI or RC models. The system toward PG 1216+069 at $z = 0.12389$ (system 3) is consistent with the expected values for CIs when comparing to C IV and Si IV; however, the system toward PG 1116+215 (system 1) and the one at $z = 0.12360$ toward PG 1216+069 (system 2) only match when comparing to C IV and Si IV, respectively. System 2 is also on the border of the predicted ratios of the TML models in the left panel of Figure 3, suggesting they are likely contributing to its ionization state in addition to CIs.
4. The ionization models we explore here cannot reproduce the ratios of the cloud along the PG 1424+240 sight line (system 4). We note that this system is near the boarder of CIs and TMLs in both panels of Figure 3, which could indicate that these mechanisms are playing some role in the observed ionization state. However, other processes may also be in play since the feature is narrow, well beyond the COS line-spread function. The true uncertainty in column density is large.
5. Stacking the spectra of all absorbing clouds within the redshifts that allows for the simultaneous detection of C IV and O VI revealed faint absorption features at $>5.5\sigma$ in C IV and O VI. However, Si IV and N V were not detected at 2σ. The column density ratios of the stack are consistent with SI models, suggesting that SIs may be another prominent ionization mechanisms in the IGM, even if not in the individual clouds presented here.

From these it is clear that the IGM in the local Universe is ionized primarily by nonequilibrium processes, in particular in the outer CGM and IGM. Further investigation of these three coronal lines (C IV, N V, and O VI) in star-forming galaxies, with HST programs such as COS-MAGIC (HST-GO-17093), will shed more light on the processes which drive the ionization of the CGM and IGM.

Acknowledgments

We thank the anonymous referee for the helpful comments which improved the paper. B.K. and S.B. were supported by NASA/STScI through grants HST-GO-17093 and NSF grant 2108159. B.K. would like to thank Tyler McCabe for their fruitful discussions regarding this project. B.K., A.R., and S.B. acknowledge the native people and the land that Arizona State University's campuses are located on the Salt River Valley. The ancestral territories of Indigenous peoples, including the Akimel O'odham (Pima) and Pee Posh (Maricopa) Indian Communities, whose care and keeping of these lands allows us to be here today.

Facilities: HST (COS); MAST.

Software: `matplotlib` (v3.2.2; Hunter 2007), `astropy` (v4.2.1; Astropy Collaboration et al. 2013, 2018), `CLOUDY` (v.17; Ferland et al. 2017), `numpy` (v1.22.0; Harris et al. 2020), `scipy` (v1.6.2; Virtanen et al. 2020), and `pandas` (v1.3.5; Reback et al. 2021).

Appendix

Here we show the spectrum and associated Voigt profile fits of our systems. The sight lines PG 1116+215, PG1216+069, PG 1424+240, and PKS 0637-752 are shown in Figures A1, A2, A3, and A4, respectively.

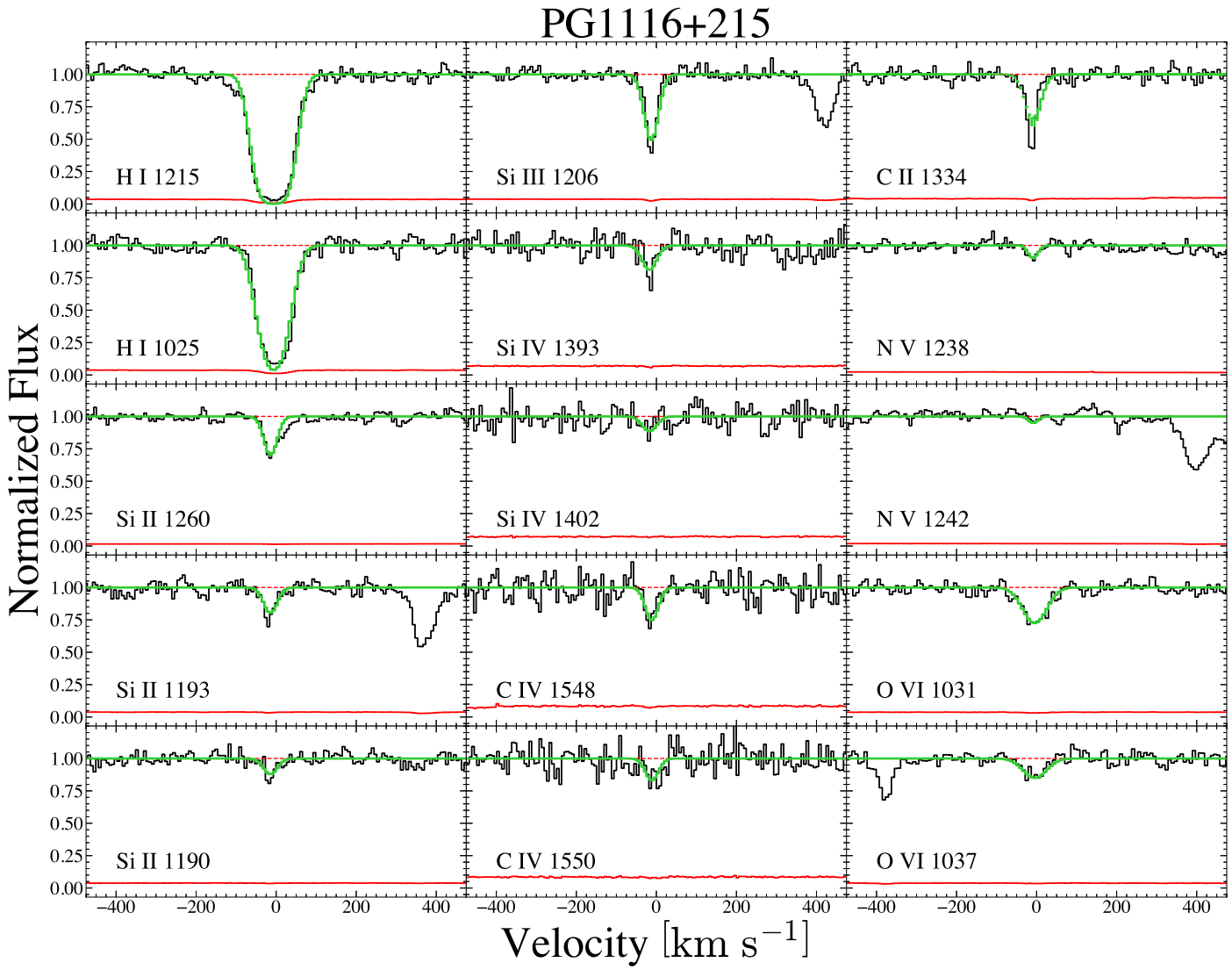

Figure A1. Normalized spectrum of the absorbing cloud along the sight line to PG 1116+215. Each panel was centered on the Lyα velocity of the cloud before fitting. The normalized flux and uncertainties are shown in black and red, respectively. The associated Voigt profile fits are shown in green. Intervening absorbers near v_{sys} that are different from the ion being plotted are labeled in blue.

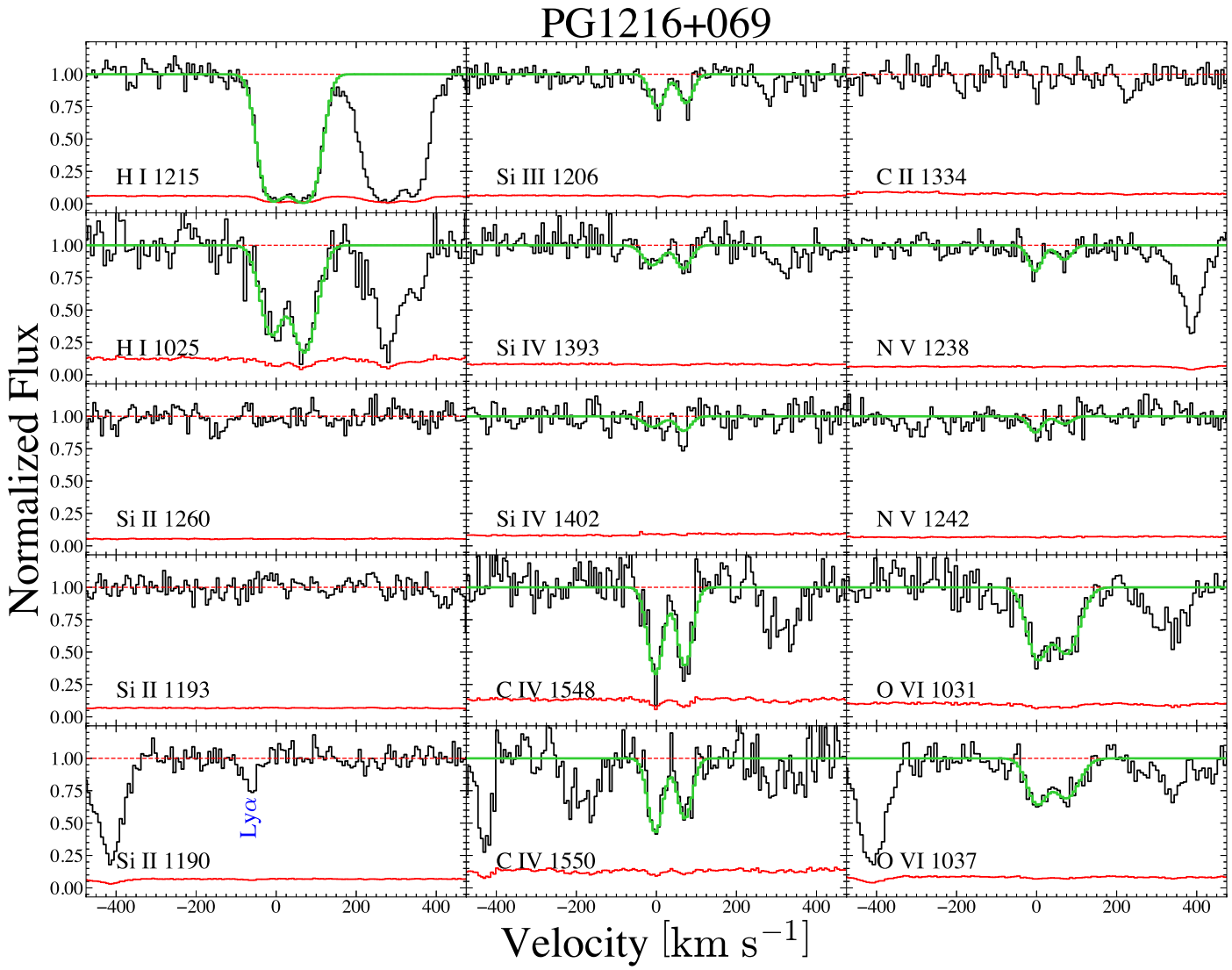

Figure A2. Same as Figure A1, but for the absorbing clouds along the sight line to PG 1216+069.

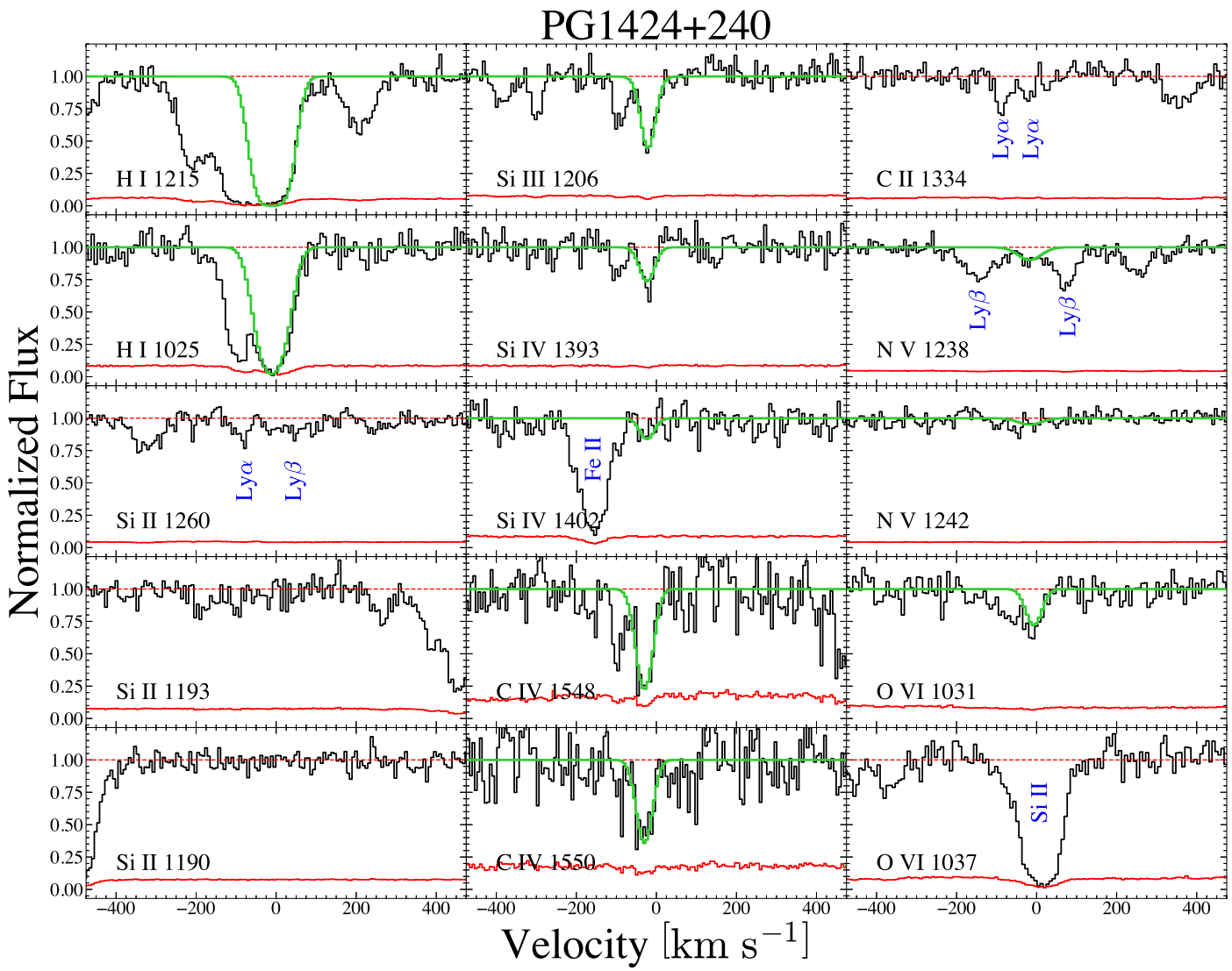

Figure A3. Same as Figure A1, but for the absorbing cloud along the sight line to PG 1424+240.

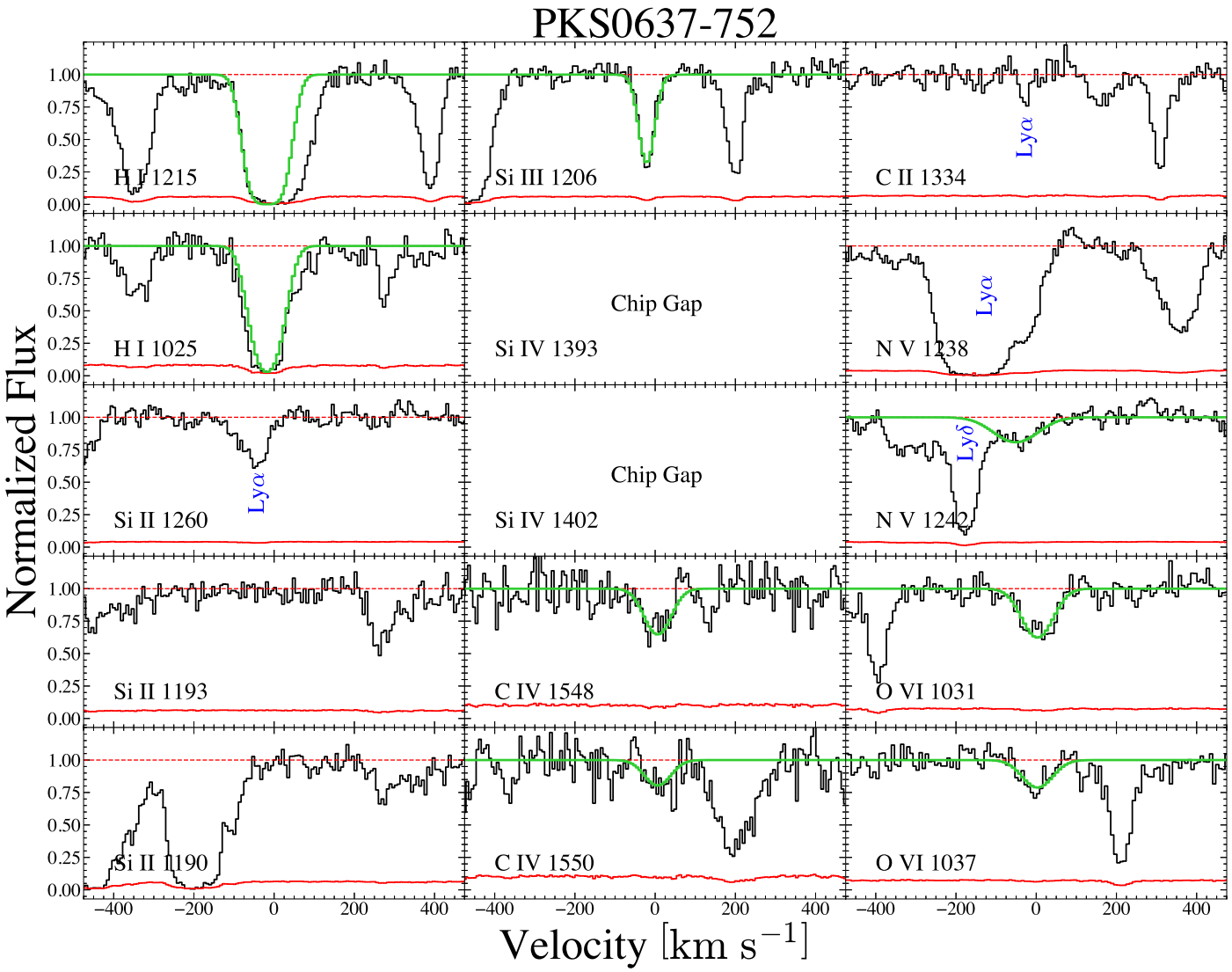

Figure A4. Same as Figure A1, but for the absorbing cloud along the sight line to PKS 0637–752.

ORCID iDs

Brad Koplitz https://orcid.org/0000-0001-5530-2872
Anjali Ramesh https://orcid.org/0000-0001-5155-8862
Sanchayeeta Borthakur https://orcid.org/0000-0002-2724-8298

References

Adelberger, K. L., Shapley, A. E., Steidel, C. C., et al. 2005, ApJ, 629, 636
Aguirre, A., Dow-Hygelund, C., Schaye, J., & Theuns, T. 2008, ApJ, 689, 851
Ahoranta, J., Finoguenov, A., Bonamente, M., et al. 2021, A&A, 656, A107
Aracil, B., Petitjean, P., Pichon, C., & Bergeron, J. 2004, A&A, 419, 811
Asplund, M., Grevesse, N., Sauval, A. J., & Scott, P. 2009, ARA&A, 47, 481
Astropy Collaboration, Price-Whelan, A. M., Sipőcz, B. M., et al. 2018, AJ, 156, 123
Astropy Collaboration, Robitaille, T. P., Tollerud, E. J., et al. 2013, A&A, 558, A33
Banerjee, E., Muzahid, S., Schaye, J., Johnson, S. D., & Cantalupo, S. 2023, MNRAS, 524, 5148
Begelman, M. C., & Fabian, A. C. 1990, MNRAS, 244, 26P
Bergeron, J., Petitjean, P., Sargent, W. L. W., et al. 1994, ApJ, 436, 33
Borkowski, K. J., Balbus, S. A., & Fristrom, C. C. 1990, ApJ, 355, 501
Borthakur, S. 2022, ApJ, 924, 123
Borthakur, S., Heckman, T., Strickland, D., Wild, V., & Schiminovich, D. 2013, ApJ, 768, 18
Cen, R., & Ostriker, J. P. 1999, ApJ, 514, 1
Cen, R., & Ostriker, J. P. 2006, ApJ, 650, 560
Chen, H.-W., & Mulchaey, J. S. 2009, ApJ, 701, 1219
Chen, H.-W., Prochaska, J. X., Bloom, J. S., & Thompson, I. B. 2005, ApJL, 634, L25
Danforth, C. W., Keeney, B. A., Tilton, E. M., et al. 2016, ApJ, 817, 111
Danforth, C. W., & Shull, J. M. 2008, ApJ, 679, 194
Davé, R., Cen, R., Ostriker, J. P., et al. 2001, ApJ, 552, 473
Davé, R., Hellsten, U., Hernquist, L., Katz, N., & Weinberg, D. H. 1998, ApJ, 509, 661
Decataldo, D., Shen, S., Mayer, L., Baumschlager, B., & Madau, P. 2023, arXiv:2306.03146
Dekel, A., & Birnboim, Y. 2006, MNRAS, 368, 2
Dekel, A., Birnboim, Y., Engel, G., et al. 2009, Natur, 457, 451
Dopita, M. A., & Sutherland, R. S. 1996, ApJS, 102, 161
Edgar, R. J., & Chevalier, R. A. 1986, ApJL, 310, L27
Ferland, G. J., Chatzikos, M., Guzmán, F., et al. 2017, RMxAA, 53, 385
Fox, A. J., Wakker, B. P., Savage, B. D., et al. 2005, ApJ, 630, 332
Gatuzz, E., García, J. A., Churazov, E., & Kallman, T. R. 2023, MNRAS, 521, 3098
Gnat, O., & Sternberg, A. 2007, ApJS, 168, 213
Gnat, O., Sternberg, A., & McKee, C. F. 2010, ApJ, 718, 1315
Green, J. C., Froning, C. S., Osterman, S., et al. 2012, ApJ, 744, 60
Haardt, F., & Madau, P. 2012, ApJ, 746, 125
Hafen, Z., Stern, J., Bullock, J., et al. 2022, MNRAS, 514, 5056
Haislmaier, K. J., Tripp, T. M., Katz, N., et al. 2021, MNRAS, 502, 4993
Harris, C. R., Millman, K. J., van der Walt, S. J., et al. 2020, Natur, 585, 357
Heckman, T., Borthakur, S., Wild, V., Schiminovich, D., & Bordoloi, R. 2017, ApJ, 846, 151
Heckman, T. M., Norman, C. A., Strickland, D. K., & Sembach, K. R. 2002, ApJ, 577, 691
Hunter, J. D. 2007, CSE, 9, 90
Jannuzi, B. T., Bahcall, J. N., Bergeron, J., et al. 1998, ApJS, 118, 1
Ji, S., Oh, S. P., & Masterson, P. 2019, MNRAS, 487, 737
Johnson, S. D., Chen, H.-W., Mulchaey, J. S., Schaye, J., & Straka, L. A. 2017, ApJL, 850, L10
Kereš, D., Katz, N., Weinberg, D. H., & Davé, R. 2005, MNRAS, 363, 2
Kravtsov, A. V. 2013, ApJL, 764, L31
Kwak, K., Shelton, R. L., & Henley, D. B. 2015, ApJ, 812, 111
Lehner, N., Berek, S. C., Howk, J. C., et al. 2020, ApJ, 900, 9
Lehner, N., Savage, B. D., Richter, P., et al. 2007, ApJ, 658, 680
Lopez, S., Reimers, D., Rauch, M., Sargent, W. L. W., & Smette, A. 1999, ApJ, 513, 598
Martin, C. L. 1999, ApJ, 513, 156
Martin, C. L., Scannapieco, E., Ellison, S. L., et al. 2010, ApJ, 721, 174
McQuinn, M. 2016, ARA&A, 54, 313
Meiksin, A. A. 2009, RvMP, 81, 1405
Méndez-Hernández, H., Cassata, P., Ibar, E., et al. 2022, A&A, 666, A56
Morrison, S., Pieri, M. M., Som, D., & Pérez-Ràfols, I. 2021, MNRAS, 506, 5750
Morton, D. C., York, D. G., & Jenkins, E. B. 1988, ApJS, 68, 449
Muzahid, S., Fonseca, G., Roberts, A., et al. 2018, MNRAS, 476, 4965
Muzahid, S., Srianand, R., Bergeron, J., & Petitjean, P. 2012, MNRAS, 421, 446
Muzahid, S., Srianand, R., & Petitjean, P. 2011, MNRAS, 410, 2193
Narayanan, A., Wakker, B. P., & Savage, B. D. 2009, ApJ, 703, 74
Nelson, D., Pillepich, A., Springel, V., et al. 2019, MNRAS, 490, 3234
Oppenheimer, B. D., Crain, R. A., Schaye, J., et al. 2016, MNRAS, 460, 2157
Oppenheimer, B. D., Davé, R., Katz, N., Kollmeier, J. A., & Weinberg, D. H. 2012, MNRAS, 420, 829
Osterman, S., Green, J., Froning, C., et al. 2011, Ap&SS, 335, 257
Pachat, S., Narayanan, A., Khaire, V., et al. 2017, MNRAS, 471, 792
Peeples, M. S., Werk, J. K., Tumlinson, J., et al. 2014, ApJ, 786, 54
Pieri, M. M., Schaye, J., & Aguirre, A. 2006, ApJ, 638, 45
Reback, J., Jbrockmendel, McKinney, W., et al. 2021, pandas-dev/pandas: Pandas v1.3.5, Zenodo, doi:10.5281/zenodo.5774815
Richter, P., Savage, B. D., Tripp, T. M., & Sembach, K. R. 2004, ApJS, 153, 165
Sankar, S., Narayanan, A., Savage, B. D., et al. 2020, MNRAS, 498, 4864
Savage, B. D., Lehner, N., Wakker, B. P., Sembach, K. R., & Tripp, T. M. 2005, ApJ, 626, 776
Savage, B. D., & Sembach, K. R. 1991, ApJ, 379, 245
Scott, J. E., Shoemaker, E. S., & Hamill, C. D. 2021, ApJ, 923, 44
Sembach, K. R., & Savage, B. D. 1992, ApJS, 83, 147
Sembach, K. R., Tripp, T. M., Savage, B. D., & Richter, P. 2004, ApJS, 155, 351
Shull, J. M., Smith, B. D., & Danforth, C. W. 2012, ApJ, 759, 23
Simcoe, R. A., Sargent, W. L. W., & Rauch, M. 2004, ApJ, 606, 92
Slavin, J. D., Shull, J. M., & Begelman, M. C. 1993, ApJ, 407, 83
Sobacchi, E., & Mesinger, A. 2013, MNRAS, 432, 3340
Somerville, R. S., & Davé, R. 2015, ARA&A, 53, 51
Steidel, C. C., Erb, D. K., Shapley, A. E., et al. 2010, ApJ, 717, 289
Tilton, E. M., Danforth, C. W., Shull, J. M., & Ross, T. L. 2012, ApJ, 759, 112
Tripp, T. M., Sembach, K. R., Bowen, D. V., et al. 2008, ApJS, 177, 39
Turner, M. L., Schaye, J., Steidel, C. C., Rudie, G. C., & Strom, A. L. 2014, MNRAS, 445, 794
Virtanen, P., Gommers, R., Oliphant, T. E., et al. 2020, NatMe, 17, 261
Wang, P., & Abel, T. 2008, ApJ, 672, 752